Characterization of early-stage cutaneous radiation injury by using optical coherence tomography angiography

JUNGBIN LEE,[1] [ID] WON HYUK JANG,[2] [ID] SEHWAN SHIM,[3] BUMJU KIM,[2] WON-SUK JANG,[4] JAE KYUNG MYUNG,[3,4,5] SUNHOO PARK,[3,4,5,6] AND KI HEAN KIM[1,2,7]

[1]*Department of Mechanical Engineering, Pohang University of Science and Technology, 77 Cheongam-Ro, Nam-gu, Pohang, Gyeongbuk 37673, South Korea*
[2]*Divison of Integrative Biosciences & Biotechnology, Pohang University of Science and Technology, 77 Cheongam-Ro, Nam-gu, Pohang, Gyeongbuk 37673, South Korea*
[3]*National Radiation Emergency Medical Centre, Korea Cancer Centre Hospital, Korea Institute of Radiological & Medical Sciences (KIRAMS), 75 Nowon-ro, Nowon-gu, Seoul 01812, South Korea*
[4]*Laboratory of Experimental Pathology, Korea Cancer Centre Hospital, Korea Institute of Radiological & Medical Sciences (KIRAMS), 75 Nowon-ro, Nowon-gu, Seoul 01812, South Korea*
[5]*Department of Pathology, Korea Cancer Centre Hospital, Korea Institute of Radiological & Medical Sciences (KIRAMS), 75 Nowon-ro, Nowon-gu, Seoul 01812, South Korea*
[6]*sunhoo@kcch.re.kr*
[7]*kiheankim@postech.ac.kr*

Abstract: Cutaneous radiation injury (CRI) is a skin injury caused by exposure to high dose ionizing radiation (IR). Diagnosis and treatment of CRI is difficult due to its initial clinically latent period and the following inflammatory bursts. Early detection of CRI before clinical symptoms will be helpful for effective treatment, and various optical methods have been applied with limitations. Here we show that optical coherence tomography angiography (OCTA) could detect changes in the skin during the latent period in CRI mouse models non-invasively. CRI was induced on the mouse hindlimb with exposure to various IR doses and the injured skin regions were imaged longitudinally by OCTA until the onset of clinical symptoms. OCTA detected several changes in the skin including the skin thickening, the dilation of large blood vessels, and the irregularity in vessel boundaries. Some of OCTA findings were confirmed by histology. The study results showed that OCTA could be used for early CRI detection.

1. Introduction

Cutaneous radiation injury (CRI) is an injury to the skin and underlying tissues caused by exposure to high dose ionizing radiation (IR) [1]. CRI involves immediate damage to continuously dividing cells including basal keratinocytes and hair follicle stem cells, followed by inflammation [2–4]. CRI has a specific characteristic of the delayed onset of clinical symptoms post-irradiation, and the asymptomatic period is called the latent period [1,5–7]. The symptoms of CRI become visible after the latent period, and these include erythema, edema, pigment changes, dry and moist desquamation, ulceration, and necrosis depending on the severity [8]. There is no effective preventive measure or treatment of CRI currently available, except for conventional conservative managements [9]. Diagnosis and treatment based on visible clinical symptoms would be late due to the successive and unpredictable inflammatory bursts. Early management of CRI would be beneficial to minimize the expansion of injured areas and to increase the treatment efficacy. Therefore, non-invasive early diagnosis of CRI would be important.

   Optical imaging methods allow non-invasive and sensitive detection of local changes in the skin, and various optical techniques have been tested for early CRI detection. 3D optical

microscopies such as reflectance confocal microscopy (RCM) and two-photon microscopy (TPM) showed the potential for early detection by observing cellular changes during the latent period. RCM detected spongiosis, exocytosis, and infiltration of inflammatory cells in the skin dermis before the appearance of clinical signs in acute radiation dermatitis [10,11]. Both RCM and TPM detected damage of epidermal cells and sebaceous glands during the clinically latent period in CRI mouse models [5,6,12]. Although microscopic techniques demonstrated sensitive detection, relatively small field of view (FOV) may limit the area of screening in practical situations. Microcirculatory network, responsible for the transport and exchange of oxygen, nutrients, and other molecules to tissues, is affected by CRI. Hyperspectral imaging (HIS) [13,14] and diffuse optical spectroscopy [15,16] detected changes in the perfusion and oxygenation of vasculature during the clinically latent period. Laser Doppler flowmetry measured perfusion changes caused by CRI [17]. These methods measured functional changes of vasculature associated with CRI. Optical imaging methods, which can visualize blood vessels, could assess morphological changes of vasculature. Optical coherence tomography angiography (OCTA), which can visualize both the microstructure and vasculature of skin non-invasively based on light reflection, has been applied to various dermatology studies [18–21]. OCTA detected the increase of skin thickness and blood vessel density as acute responses to ultraviolet radiation [19]. OCTA visualized capillary-level vascular and structural changes in subjects with pathological conditions such as psoriasis, chronic graft-versus-host-disease, and scleroderma [20,21]. OCTA was applied to a CRI study previously and it detected the degeneration and regeneration of vasculature in the mouse ear pinna at the early stage after whole body gamma irradiation [22].

In this study, OCTA was used to observe both the structural and vascular changes in skin by CRI at the early stage in a local-irradiation mouse model. Various doses of 0 Gy (control), 10 Gy, 20 Gy, and 40 Gy were irradiated on the mouse hindlimb and the irradiated skin regions were imaged longitudinally by OCTA until the onset of clinical symptoms. Changes in the skin were analyzed both qualitatively and quantitatively in comparison with bright-field imaging and histology.

2. Materials and method

2.1. Mouse model preparation

The experimental procedure was approved by the Institutional Animal Care and Use Committee (IACUC, KIRAMS2015-0004) of Korea Institute of Radiobiology & Medical Sciences (KIRAMS). All experiments were carried out in accordance with the approved guidelines and regulations. Six-week-old male hairless mice (SKH1-HrHr, ORIENT BIO Inc, Korea) were used in this study. Mice were divided into four groups: a control group (0 Gy, n = 5) and irradiated groups exposed to 10 Gy, 20 Gy, and 40 Gy (n = 6 each) doses, respectively. Mice were irradiated with the same protocol as a previous study [6]. In brief, anesthetized mice were irradiated onto the hindlimb by using a biological irradiator (XRAD-320, PRECISION X-RAY, Softex, Korea). The irradiation was single exposure to X-ray at a dose rate of 2 Gy/min. The reference dose rate was established with an UNIDOSE E universal dosimeter (PTW, Freiburg, Germany) in realistic irradiation conditions in air on the animal plate. After the irradiation, the mice were maintained under constant temperature (23 ± 1 °C) and photoperiod (12 hours of light, 12 hours of dark). Regular chow and 3-stage filtered water were provided to the mice freely. OCTA imaging was started from day 2 post-irradiation to monitor changes caused by CRI. Both bright-field imaging and OCTA were performed daily until the onset of clinical symptoms. During the OCTA imaging, mice were anesthetized using a face mask administering a gas mixture of 1.5%/vol isoflurane (Terrel, Piramal) and medical grade oxygen. The body temperature was maintained at 37°C using a temperature-controlled heating plate (Chamlide TR, Live Cell Instruments, Korea). For the minimization of motion artifacts during OCTA imaging, a custom-made hindlimb holder and surgical tape were used to hold the hindlimb and to stretch the hindlimb skin [6].

2.2. OCT angiography and bright-field imaging

Optical configuration of the OCTA system was based on a previous OCT setup [23]. Briefly, a wavelength-swept source (SSOCT-1310, Axsun Technologies) was used as the light source, and it had the repetition rate of 50 kHz, center wavelength of 1310 nm, bandwidth of 107 nm, and imaging depth of 6 mm in air. Light from the source was split into the sample and reference arms of an interferometer. In the sample arm, light was collimated, reflected onto a galvanometric 2D scanner (GVS012, Thorlabs), and transmitted through a 5× OCT scan lens (LSM03, EF = 36 mm, Thorlabs) for scanning the sample. Reflected light from the sample was combined with reflected light from the reference arm at the detection arm. Interference signals of combined light were collected at a balanced photodetector (PDB410C, Thorlabs), and digitized by a DAQ board (ATS9350-2G, Alazartech) after a low pass filter (PLP90, Mini-circuits). Difference of light dispersion between the reference and sample arms was compensated numerically by using pre-calibration data obtained with a mirror sample. OCT had the image resolution of 20 μm and 10.8 μm in the transverse and axial directions, respectively. The imaging FOV was 4 mm × 4 mm × 2.25 mm in the x, y, and z directions, consisting of 500 pixels × 500 pixels × 320 pixels. For OCTA imaging, the cross-sectional imaging in the x-z plane was repeated 10 times and the repeated images processed by using the complex differential variance (CDV) algorithm [24]. OCTA images were presented in the en-face plane as the maximum intensity projection (MIP) of volumetric angiography data. In order to observe the same hindlimb skin regions longitudinally, the OCTA scanning area was carefully aligned to be around a midpoint of the right hip and knee joints. Because the hindlimb area (approximately 1 cm^2) was not much wider than the OCT FOV (4 mm × 4 mm), it was possible to image the same skin regions repeatedly. The total imaging time was approximately 50s per volume. Custom software was used to acquire OCT images with real-time display. Both cross-sectional OCT and en-face OCTA MIP images were processed and analyzed post-acquisition by using MATLAB (Matlab 2016a, Mathworks).

Bright-field images of the mouse hindlimb skin were acquired daily to monitor clinically visible changes in the CRI mouse models. Bright-field images were acquired just before the OCTA imaging of the mouse models under respiratory anesthesia. Bright-field imaging was performed under identical environmental conditions including standard room lighting and fixed sample and camera positions throughout the experiment. A metric ruler was imaged together with the mouse hindlimb as the scale reference.

2.3. Quantitative analysis of skin thickness and vasculature

Thickness of the mouse hindlimb skin including both the skin epidermis and dermis was measured by analyzing cross-sectional OCT images. The skin thickness was measured as a vertical distance from the skin surface to the bottom of dermis. Average skin thickness was calculated by using approximately 100 equal-distanced thickness measurements from each volumetric OCT image. At least 4 mouse data out of 5-6 mouse data was valid for each group in all the experiment days, and the average and standard deviation (SD) were calculated. The measurement results were displayed as the relative thickness with respect to the average thickness of 0 Gy mouse skins.

Vasculature in the skin was analyzed from en-face OCTA images. Diameters of large blood vessels and the irregularity in vessel boundaries were measured. In the measurement of vessel diameter, the vessel was skeletonized first to find the center line and orientation. Diameter of the vessel was obtained by measuring line widths perpendicular to the vessel center line and then by averaging the line widths along the vessel center line [25,26]. The line width was the full width at half maximum (FWHM) of the profile. Changes in vessel diameter were analyzed by tracking identical blood vessels in longitudinal OCTA images. The change in vessel diameter was presented as the ratio of the diameter on day 6 post-irradiation to the one on day 2 post-irradiation. More than three blood vessels were tracked, and the changes were averaged. The irregularity of blood vessel boundaries was analyzed by calculating the coefficient of variation (CV) of the

vessel line widths along the vessel. CV is defined as a ratio of the standard deviation (SD) to the mean, and represents the standardized measure of dispersion. Relatively small CV values indicate smooth vessel boundaries, while large CV values do irregular vessel boundaries with high variations in vessel diameter. More than 10 large blood vessels, which ran at least 200 μm in length without branching out, were selected and used in the CV analysis.

Statistical analysis (statistical significance) was performed by using GraphPad Prism 7 (GraphPad Software Inc., La Jolla, CA). Welch's t-test was used to assess the difference in the average values between the groups with unequal variances or unequal sample sizes. All statistical tests were performed by two-tailed tests, and p-values < 0.05 were considered as the criteria for statistical significance. Results were expressed as mean ± SD. Statistical significance was presented by the number of asterisks depending on the p-value; $*p \leq 0.05$, $**p \leq 0.01$, $***p \leq 0.001$, $**** p \leq 0.0001$. The results were plotted by using Origin (Origin 9.0, OriginLab).

2.4. Skin tissue histology

Histology of the CRI mouse skins was performed on day 6 post irradiation, one CRI mouse for each group. Mice were anesthetized, euthanized, and necropsied, and the hindlimb skins were excised and fixed with 4% paraformaldehyde solution for 24 hours. After the fixation, the skin tissues were embedded in paraffin wax and were sectioned in 4 μm thickness. The sections were stained with hematoxylin and eosin (H&E) and examined to access microscopic cellular information.

3. Results

3.1. Longitudinal bright-field images of CRI mouse hindlimb skins

The irradiated skin regions of CRI hairless mouse models were observed longitudinally by bright-field imaging. Representative longitudinal bright-field images of the CRI mouse hindlimb skins with 0 Gy (control), 10 Gy, 20 Gy, and 40 Gy irradiation doses are shown in Fig. 1. The longitudinal bright-field images are on every two days post-irradiation. In the 0 Gy (control) mouse, the bright-field images showed typical features of normal hairless mouse skin: pale skin with sparse hair distribution. In the irradiated mice, the bright-field images showed some changes from day 4 post-irradiation. In the 10 Gy mouse, hair loss was observed on day 4 post-irradiation and then there was no further progression. In the 20 Gy and 40 Gy mice, hair loss on day 4 post-irradiation, and then erythema and desquamation on day 8 post-irradiation were observed. The clinical symptoms were more severe in the 40 Gy mouse than in the 20 Gy one. The clinically latent period in both the 20 Gy and 40 Gy mouse models was considered until day 6 post-irradiation, because the clinical symptoms appeared on day 8. Based on the results of bright-field imaging, longitudinal OCTA imaging was performed until day 8 post-irradiation.

3.2. Representative OCTA images of high-dose CRI mouse skin in the late latent period

Longitudinal bright-field images of CRI mouse skins showed that the latent period in both the 20 Gy and 40 Gy mice was until day 6 post-irradiation. OCTA imaging was performed longitudinally throughout the latent period. In order to show changes in the skin detected by OCTA in the late latent period, representative OCTA images of a 40 Gy mouse skin on day 6 post-irradiation are presented in Fig. 2. Bright-field images, cross-sectional OCT images, and en-face OCTA images of the 0 Gy (control) and 40 Gy mouse skins are shown in Fig. 2(a – d) and (e – h), respectively. En-face OCTA images were MIP images, and two OCTA images were generated by MIP processing in two different depth ranges of 50–125 μm and 100–325 μm. In the 0 Gy (control) mouse, both the bright-field image and OCT image showed normal skin structures. The bright-field image showed the pale skin with sparse hair distribution. The cross-sectional OCT
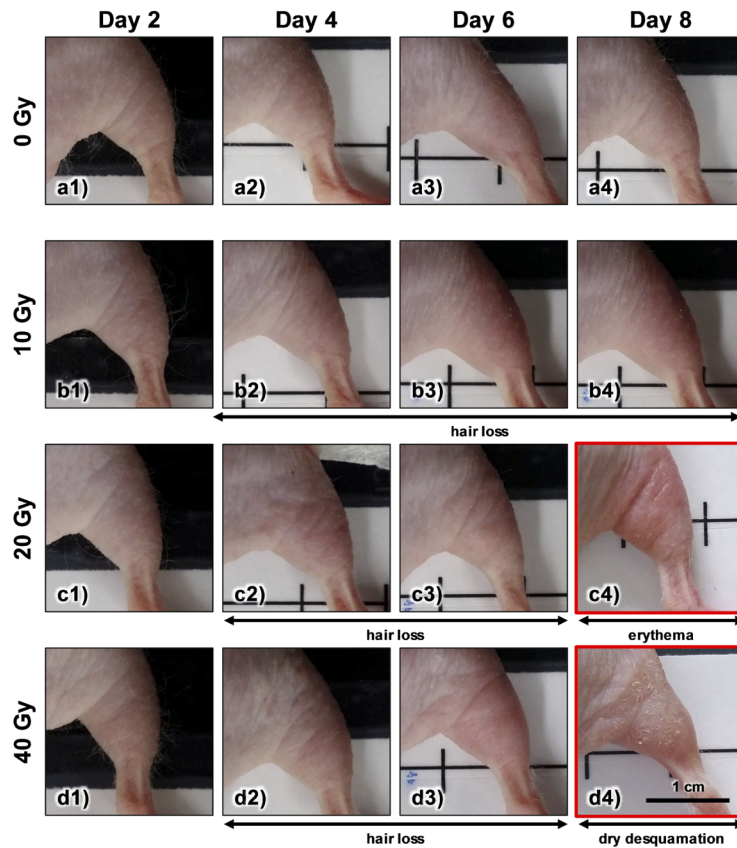
Fig. 1. Longitudinal bright-field images of CRI mouse hindlimb skins. (a-d): bright-field images of (a) 0 Gy (control), (b) 10 Gy, (c) 20 Gy, and (d) 40 Gy mouse hindlimb skins on every two days post-irradiation, respectively. Clinical diagnosis and their injury progressions are depicted below the images with horizontal black arrow lines. Outlined images with red color on day 8 post-irradiation indicate the clinically visible stages of CRI. Scale bars represent 1 cm.

image showed the thin highly scattering dermis superficially and the weakly scattering fascia or muscle layer below the dermis. Some microstructures such as hair follicles and sebaceous glands were observed in the dermis. The two en-face OCTA images showed capillaries or small vessels and relatively large vessels in the superficial and deep skin dermis, respectively. Large blood vessels had smooth boundaries. In the 40 Gy mouse, the bright-field image showed not much visible changes in the skin except hair loss on day 6 post-irradiation. However, OCTA detected several changes in the skin. The cross-sectional OCT image showed the thicker skin dermis with reduced reflection intensities compared to the 0 Gy (control) mouse skin. The muscle and fascia layer appeared at the higher depth than to the one in the 0 Gy mouse due to the thickening of skin dermis. The en-face OCTA images showed not much changes in small blood vessels in the superficial dermis in comparison to the ones in the control mouse skin, but significant changes in large blood vessels in the deep dermis. The large blood vessels were dilated and had irregular vessel boundaries. The irregular vessel boundaries could indicate leakage caused by the damage of endothelial cells. There were more branches of small and distorted blood vessels. The representative OCTA images of the 40 Gy mouse in the late latent period showed that there were structural and vascular changes in the skin caused by CRI within the latent period.
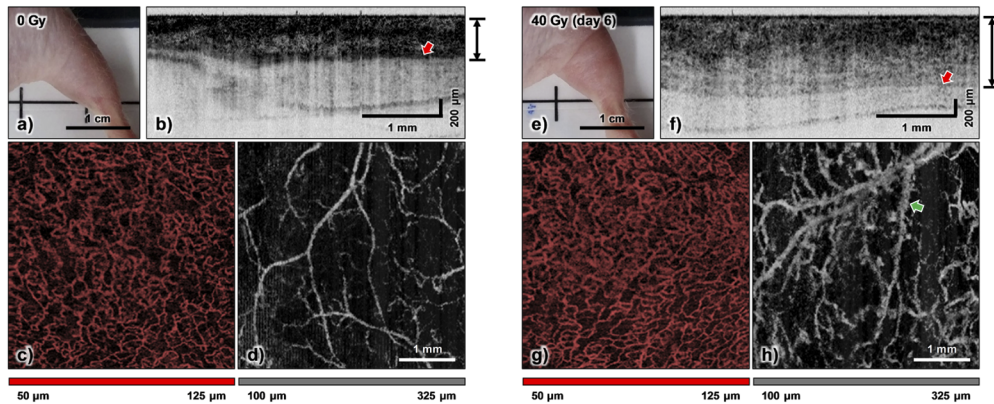
Fig. 2. Representative bright-field and OCTA images of the 0 Gy (a-d) and 40 Gy (e-h) mouse skins in late latent period (day 6 post-irradiation). In each case, a bright-field images, a cross-sectional OCT image, two en-face OCTA MIP images covering the superficial dermis (50–125 µm from the surface) and deep dermis (100–325 µm) are presented. The OCTA images of the superficial and deep dermis are depicted in red or black-white pseudo-colors, respectively. Black arrow lines on the right side of cross-sectional OCT images (b, f) mark the average thickness of skin epidermis and dermis, and red arrows in the images mark the bottom of the skin dermis. A green arrow in the en-face OCTA MIP image of the deep dermis in the 40 Gy mouse skin (h) marks the representative irregular vessel boundary.

3.3. Longitudinal changes of the skin thickness during the clinically latent period

The OCTA images of the 40 Gy mouse skin in the late latent period in Fig. 2 showed structural and vascular changes inside the skin. The changes in the CRI mouse skins were analyzed in detail by longitudinal OCTA imaging during the latent period and results are shown in Fig. 3. Representative longitudinal cross-sectional OCT images of 0 Gy (control), 10 Gy, 20 Gy, and 40 Gy mouse skins from day 2 to 6 post-irradiation are shown in Fig. 3(a – d), respectively (see Visualization 1). In the 0 Gy (control) mouse skin, the OCT images clearly showed normal skin structures including the superficial highly scattering dermis and weakly scattering fascia or muscle layer below. The topmost epidermis was not discerned in the OCT images, because the epidermis of mouse skin was too thin for the image resolution of the current OCT system. In the irradiated mouse skins, the longitudinal OCT images showed the thickening of skin dermis. In the 10 Gy mouse skin, the skin thickness remained about the same as the one of the 0 Gy (control) mouse skin. The boundaries between the dermis and muscle layers were clearly visible.

In the 20 Gy and 40 Gy mouse skin, the skin thickness increased with time, and reflection intensities in the dermis decreased gradually. The boundaries between the dermis and muscle layers became less clear with the decrease of reflection intensities in the skin dermis. However, it was still possible to find the boundaries during the latent period. The skin thickening during the observation period was quantitatively analyzed, and the results are shown in Fig. 4. The measured skin thicknesses of 0 Gy (black), 10 Gy (green), 20 Gy (blue), and 40 Gy (red) mouse skins were presented in different color markers. In the 0 Gy (control) mice, constant skin thicknesses were observed during the imaging period. The skin thicknesses of the 10 Gy mice also remained constant similarly to those of the 0 Gy mice. However, the increase of skin thickness was observed in both the 20 Gy and 40 Gy mice. The skin thicknesses increased gradually and the ones on day 4 post-irradiation were significantly higher than the ones of 0 Gy mouse skins. On day 6 post-irradiation, the skin thicknesses of 20 Gy and 40 Gy mice were approximately 1.49 and 1.62 times of the ones of 0 Gy mouse skins, respectively. The cause of skin thickening was not known,
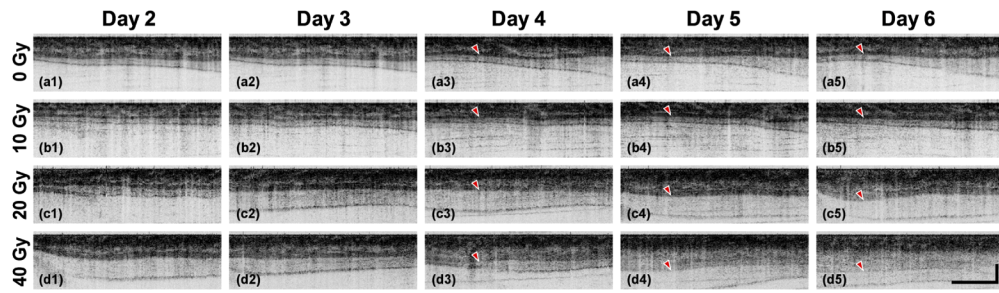
Fig. 3. Longitudinal cross-sectional OCT images of CRI mouse skins during the clinically latent period. (a-d): longitudinal OCT images of (a) 0 Gy (control), (b) 10 Gy, (c) 20 Gy, and (d) 40 Gy mouse skins, respectively (see Visualization 1). Red arrowheads mark the bottoms of the skin dermis. Scale bars represent 1 mm and 400 μm in the lateral (x) and axial (z) directions, respectively.

but it could be due to the damage and leakage of blood vessels. The analysis results showed that OCTA could detect the progression of CRI during the latent period.
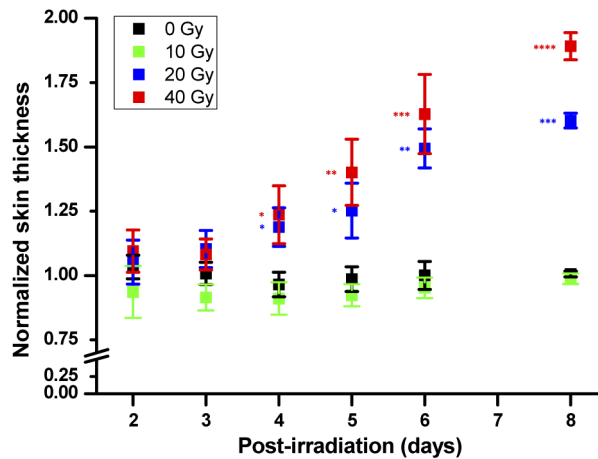

Fig. 4. Quantitative analysis of the skin thickening in cross-section intensity OCT images. The skin thicknesses including both the epidermis and dermis in 0 Gy (black), 10 Gy (green), 20 Gy (blue), and 40 Gy (red) are presented in different color-markers, respectively. The skin thicknesses were normalized by the average one in 0 Gy mice. Statistical significances were presented by number asterisks depending on the p-value: $*p \leq 0.05$, $**p \leq 0.01$, $***p \leq 0.001$, $****p \leq 0.0001$.

3.4. Histology of the CRI mouse skin in the late latent period

For the confirmation of structural changes detected by OCTA, the hindlimb skins of CRI mouse models were processed for histology with hematoxylin and eosin (H&E) staining. Histology results of 0 Gy (control), 10 Gy, 20 Gy, and 40 Gy mouse skins on day 6 post-irradiation are shown in Fig. 5(a – d), respectively. The histological image of 0 Gy (control) mouse skin showed normal skin structures: thin epidermis and dermis, regularly distributed hair follicles and sebaceous glands in the dermis, and underlying muscles. The histological image of 10 Gy mouse skin also showed the normal skin structures, similarly to the one of 0 Gy (control) mouse skin. The histological images of both 20 Gy and 40 Gy mouse skins showed several changes.

Both the epidermis and dermis were thickened. Cells in the epidermis and cell clusters in the sebaceous glands and hair follicles were damaged. There were inflammatory cells infiltrated in the dermis. These changes were more severe with the higher irradiation dose. These histological images showed detailed cellular changes by CRI and confirmed the OCTA observation of skin thickening.
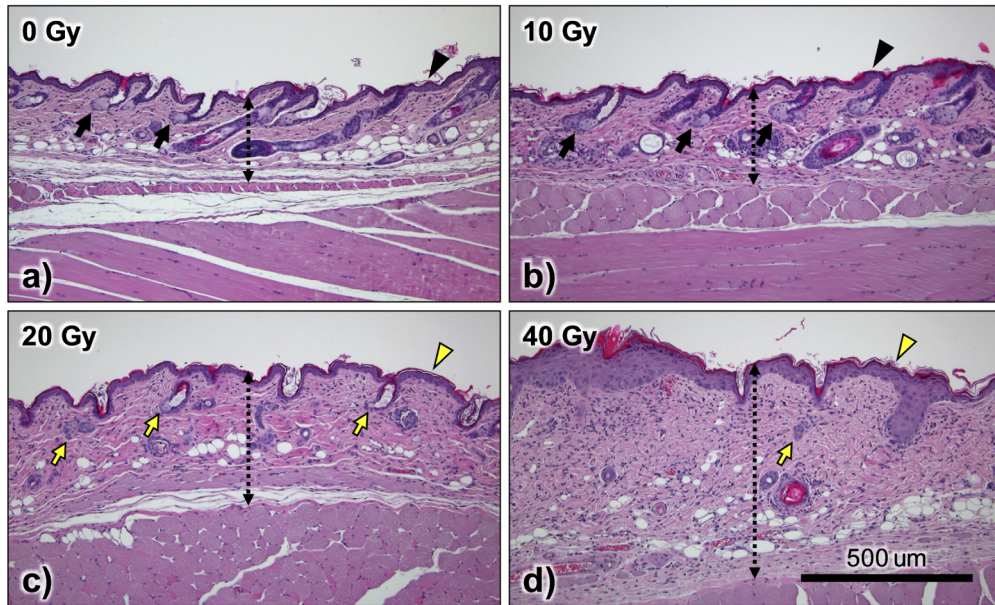

Fig. 5. Histology images of CRI mouse skins in late latent stage (day 6 post-irradiation). (a-d): hematoxylin and eosin (H&E) stained histology images of 0 Gy (control), 10 Gy, 20 Gy, and 40 Gy mouse skins, respectively. Black arrowheads and arrows mark the thin epidermis and normal sebaceous glands, respectively. Yellow arrowheads and arrows mark the thickened epidermis and partially or completely damaged hair follicles and sebaceous glands. Black dotted lines with arrows mark the depth range of the epidermis and dermis. A scale bar represents 500 μm.

3.5. *Longitudinal changes of vasculature in the skin during the latent period*

Another feature in the CRI mouse skin detected by OCTA in the late latent period was the changes of large blood vessels in the deep skin dermis. Early-stage changes of large blood vessels were monitored in detail by longitudinal OCTA imaging during the latent period. Representative longitudinal OCTA images of large blood vessels in 0 Gy (control), 10 Gy, 20 Gy, and 40 Gy mouse skins are shown in Fig. 6(a – d), respectively. Longitudinal OCTA imaging was performed approximately in the same skin regions so that the same blood vessels could be observed multiple times. En-face OCTA MIP images were generated from the depth range of 100 μm – 325 μm from the skin surface, and the depth range for MIP processing was manually adjusted in the thickened skin cases. The OCTA images of the 0 Gy (control) mouse skin showed the typical vasculature in the deep dermis. Large blood vessels were approximately 100 μm in diameter and the vessel diameter decreased with branching. Blood vessels were straight and smooth on the boundary. In the 10 Gy mouse skin, OCTA images showed similar blood vessel morphologies as the ones in the 0 Gy (control) mouse skin. Although there was a slight increase of blood vessel branches on day 5 post-irradiation, the diameter and shape of large blood vessels remained the same. In the 20 Gy and 40 Gy mouse skins, OCTA images detected progressive changes of

large blood vessels with time. The blood vessels were dilated, and the vessel boundaries became irregular. There were more branches of small and distorted blood vessels with time. In the 20 Gy mouse skin, large blood vessels appeared normal on day 2 post irradiation. Then, the vessel dilation and boundary irregularity appeared on day 3 and later. In the 40 Gy mouse skin, large blood vessels were relatively thin and locally dilated on day 2 post irradiation. More distorted vessels appeared on day 3, and then the local dilation and boundary irregularity spread on later days of the latent period.
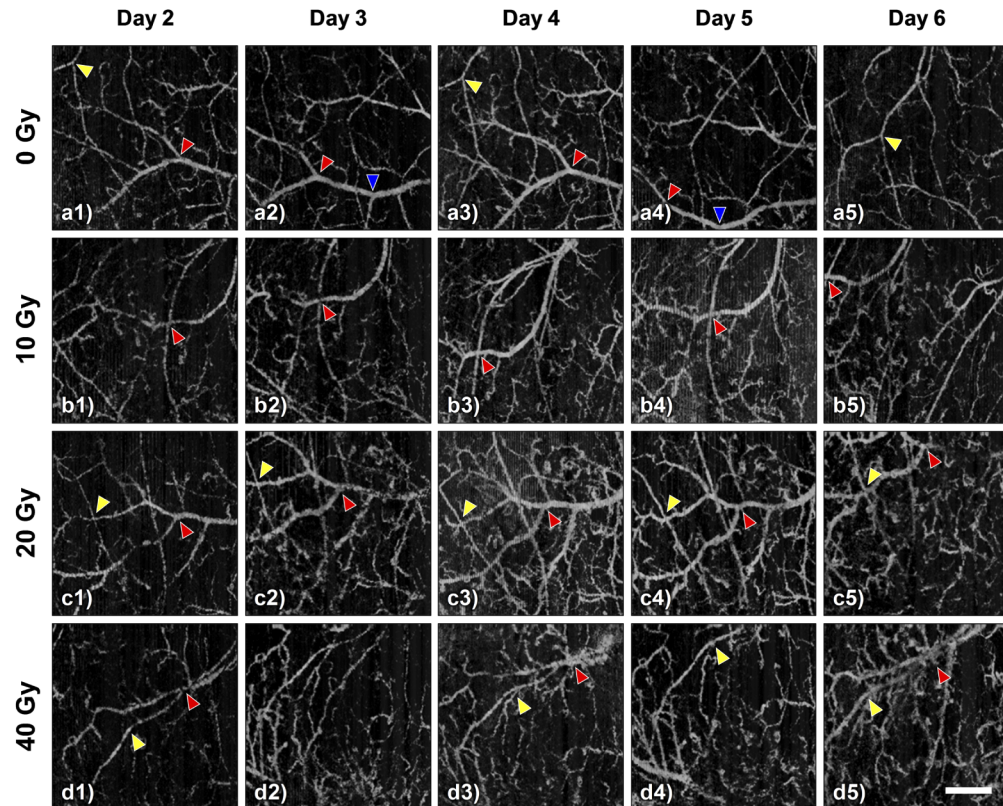

Fig. 6. Longitudinal en-face OCTA MIP images of large blood vessels in the deep skin dermis of CRI mice during the latent period. (a - d): longitudinal OCTA images of 0 Gy (control), 10 Gy, 20 Gy, and 40 Gy mouse skins, respectively. Arrowheads in various colors mark identical blood vessels in multiple images. The scale bar represents 1 mm.

The changes in the diameter and boundary irregularity of large blood vessels in the 40 Gy mouse skins were quantified by analyzing the longitudinal OCTA images, and the results are shown in Fig. 7. Representative OCTA images of 0 Gy and 40 Gy mouse skins on day 2 and 6 post-irradiation are shown in Fig. 7(a-b) and (c-d), respectively. Magnified OCTA images showed large blood vessels used in the analysis. The vessel in the 0 Gy mouse skin images looked straight with clear boundaries on both days. On the other hand, the vessel in the 40 Gy mouse skin images was relatively straight on day 2 post-irradiation and became enlarged and irregular on day 6. The analysis results of vessel diameter and the boundary irregularity during the latent period are shown in Fig. 7(e) and (f). The average diameter of large vessels in 40 Gy mouse skins was 1.43 ± 0.05 times high on day 6 post-irradiation compared to the one on day 2 post-irradiation. The CV values, representing the irregularity in vessel boundaries, was approximately 0.14 in the 0 Gy mouse skins. In the 40 Gy mouse skins, the CV value of the

vessel boundaries increased with time and was significantly high (0.23) on day 6 post-irradiation compared to the one in the 0 Gy mouse skins. The analysis results showed that both the diameter and boundary irregularity in large blood vessels changed significantly in the 40 Gy mouse skins during the latent period, and OCTA could detect the vascular changes.
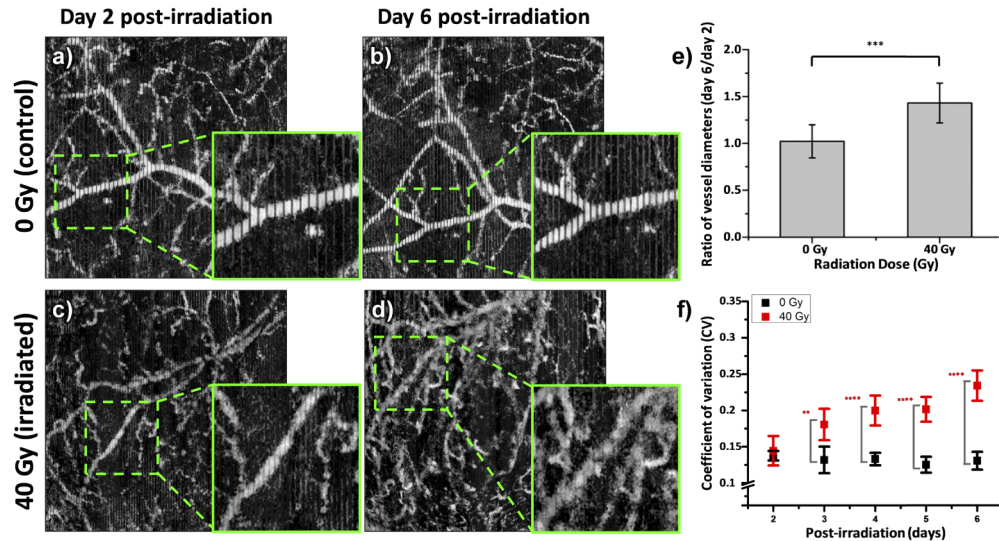

Fig. 7. OCTA images of large blood vessels in 0 Gy and 40 Gy mouse skins at two different time points of the latent period and the quantitative analysis of vascular changes. (a-d): OCTA images of large blood vessels in the 0 Gy (a, b) and 40 Gy (c, d) mice on day 2 and day 6 post-irradiation, respectively. Identical blood vessels detected on both days were marked with green dashed boxes. (e): relative diameters of large vessels on day 6 post-irradiation with respect to on day 2. (f): irregularity in the vessel boundaries. Statistical significances were presented by the number of asterisks depending on the p-value: **p ≤ 0.01, ***p ≤ 0.001, ****p ≤ 0.0001.

4. Discussion

OCTA is a non-invasive 3D imaging method visualizing both the microstructure and vasculature of tissues non-invasively based on light reflectance. In this study, OCTA was used to characterize structural and vascular changes in the CRI mouse skins during the initial latent period. CRI mouse models were generated by local irradiation on the hindlimb with various IR doses of 10 Gy, 20 Gy, and 40 Gy, and OCTA imaging was performed longitudinally through the latent period until the onset of clinical symptoms. The latent period of CRI was determined via the separate bright-field imaging. OCTA detected several changes in the skin of CRI mouse models exposed to high irradiation doses of 20 Gy and 40 Gy during the latent period. The changes were the skin thickening, the dilation of large blood vessels, and the irregularity in vessel boundaries. Such changes were not observed in the skin exposed to low irradiation dose of 10 Gy. The findings of OCTA in CRI mouse models were quantitatively analyzed. The skin thickening became significant from day 4 post-irradiation in the 20 Gy and 40 Gy irradiated mouse skins and progressed more on later days. The skins in the 20 Gy and 40 Gy irradiated mice on day 6 post-irradiation were thicker than the one in control mice by approximately 1.49 and 1.62 times, respectively. The dilation of large blood vessels and the irregular vessel boundaries were observed locally on day 2 to 4 post-irradiation and then spread to more of the large vessels. The skin thickening was confirmed by histology. The new OCTA findings of structural and

vascular changes in the CRI mouse model were consistent with previous reports. A longitudinal fluorescence microscopy study in a hairless mouse model with single-dose irradiation of 90 Gy on the ear showed similar results [27]. The ear skin showed the increase of permeability, the leakage of blood vessels, and the increase of arteriole and venule diameters. The skin thickening was observed previously by ultrasound imaging [28,29]. The skin thickening could be a side-effect of vascular injuries, where blood and body fluid leaked from vessels into the dermis. It could also be caused by excessive accumulation and decreased degradation of extracellular matrix (ECM) proteins, mainly collagen [30]. Advantages of OCTA in the detection of structural and vascular changes are the high imaging speed and the high imaging depth down to the skin dermis.

Although OCTA detected the structural and vascular changes in the CRI mouse skins, the features found in the current study might not be applicable to human subjects. OCTA detection of the skin thickening in human subjects could be difficult, because human skin is much thick compared to mouse skin in the normal condition and OCTA might not able to access the bottom of skin dermis in the thickened human skin cause by CRI. However, the skin epidermis was thickened as well as the skin dermis by CRI and the change in the skin epidermis should be accessible by OCTA. Longitudinal OCTA study with the CRI mouse models also showed that reflection intensities in the skin dermis decreased with the progression of skin thickening. Therefore, the OCTA measurement of the attenuation profiles in the skin dermis could be another feature to be used for early CRI detection. Such proposed ideas need to be verified with future OCTA studies with large animal models such as swine models. Although this study showed the OCTA detection of structural and vascular changes in the mouse skin during the clinically latent period, the current OCTA setup had limitations and rooms for improvement. First, the imaging speed of OCTA could be improved. The current OCTA was slow by generating vascular images at 50 seconds per volume and was sensitive to inevitable motion artifacts during in-vivo imaging. Various high-speed OCT methods have been developed up to several tens of volumes per seconds [31,32]. Such high-speed OCT systems would shorten the imaging time and avoid motion artifacts. Second, OCTA detected changes in the microstructure and vasculature of the skin by CRI. Functional changes in vasculature such as oxygen saturation, and oxy-hemoglobin and deoxy-hemoglobin concentration have been previously reported as biomarkers of the early-stage CRI by hyperspectral imaging (HSI) [14], multi-spectral imaging (MSI) [33], and spectroscopic-OCT [34,35]. Multimodal imaging by combining OCTA and the spectral imaging methods could be used to correlate between the structural and functional changes in vasculature for the precise and early detection of CRI [36,37].

5. Conclusion

OCTA was used to characterize structural and vascular changes caused by CRI in an in-vivo mouse model as a potential early detection method. OCTA detected the skin thickening and changes in large blood vessels in the mouse skin exposed to high-dose irradiation before the onset of clinical symptoms. These changes were analyzed both qualitatively and quantitatively. OCTA findings were consistent with bright-field imaging and histology. The results showed that OCTA is sensitive to early-stage changes in CRI and could be used as an early detection method.

Funding

Acknowledgment

Disclosures

The authors declare that there are no conflicts of interest related to this article.

References

1. H. Dorr and V. Meineke, "Acute radiation syndrome caused by accidental radiation exposure - therapeutic principles," BMC Med. **9**(1), 126 (2011).
2. F. A. Mendelsohn, C. M. Divino, E. D. Reis, and M. D. Kerstein, "Wound care after radiation therapy," Adv. Skin Wound Care **15**(5), 216–224 (2002).
3. M. J. Eide and M. A. Weinstock, "Association of UV index, latitude, and melanoma incidence in nonwhite populations–US Surveillance, Epidemiology, and End Results (SEER) Program, 1992 to 2001," Arch. Dermatol. **141**(4), 477–481 (2005).
4. E. Lopez, R. Guerrero, M. I. Nunez, R. del Moral, M. Villalobos, J. Martinez-Galan, M. T. Valenzuela, J. A. Munoz-Gamez, F. J. Oliver, D. Martin-Oliva, and J. M. Ruiz de Almodovar, "Early and late skin reactions to radiotherapy for breast cancer and their correlation with radiation-induced DNA damage in lymphocytes," Breast Cancer Res. **7**(5), R690–R698 (2005).
5. W. H. Jang, S. Kwon, S. Shim, W. S. Jang, J. K. Myung, S. Yang, S. Park, and K. H. Kim, "Comparison between reflectance confocal microscopy and 2-photon microscopy in early detection of cutaneous radiation injury in a mouse model in vivo," J. Biophotonics **11**(10), e201700337 (2018).
6. W. H. Jang, S. Shim, T. Wang, Y. Yoon, W. S. Jang, J. K. Myung, S. Park, and K. H. Kim, "In vivo characterization of early-stage radiation skin injury in a mouse model by two-photon microscopy," Sci. Rep. **6**(1), 19216 (2016).
7. O. Carvalho, M. Benderitter, and L. Roy, "Noninvasive radiation burn diagnosis using speckle phenomenon with a fractal approach to processing," J. Biomed. Opt. **15**(2), 027013 (2010).
8. J. L. Ryan, "Ionizing Radiation: The Good, the Bad, and the Ugly," J. Invest. Dermatol. **132**(3), 985–993 (2012).
9. M. Singh, A. Alavi, R. Wong, and S. Akita, "Radiodermatitis: A Review of Our Current Understanding," Am. J. Clin. Dermatol. **17**(3), 277–292 (2016).
10. S. Vano-Galvan, E. Fernandez-Lizarbe, M. Truchuelo, B. Diaz-Ley, E. Grillo, V. Sanchez, L. Rios-Buceta, J. Paoli, S. Sancho, A. Montero, R. Hernanz, A. Ramos, P. Jaen, and S. Gonzalez, "Dynamic skin changes of acute radiation dermatitis revealed by in vivo reflectance confocal microscopy," J. Eur. Acad. Dermatol. Venereol. **27**(9), 1143–1150 (2013).
11. J. Kisonas, J. Venius, O. Sevriukova, M. Grybauskas, K. Guogyte, A. Burneckis, and R. Rotomskis, "Application of Reflectance Confocal Microscopy for Early Diagnosis of Radiation-Induced Acute Dermatitis in Radiosensitive Patient: Case Study," Radiat. Prot. Dosim. **182**(1), 93–97 (2018).
12. R. G. B. Langley, M. Rajadhyaksha, P. J. Dwyer, A. J. Sober, T. J. Flotte, and R. R. Anderson, "Confocal scanning laser microscopy of benign and malignant melanocytic skin lesions in vivo," J. Am. Acad. Dermatol. **45**(3), 365–376 (2001).
13. M. S. Chin, B. B. Freniere, L. Lancerotto, J. Lujan-Hernandez, J. H. Saleeby, Y. C. Lo, D. P. Orgill, J. F. Lalikos, and T. J. Fitzgerald, "Hyperspectral imaging as an early biomarker for radiation exposure and microcirculatory damage," Front. Oncol. **5**, 232 (2015).
14. M. S. Chin, B. B. Freniere, Y. C. Lo, J. H. Saleeby, S. P. Baker, H. M. Strom, R. A. Ignotz, J. F. Lalikos, and T. I. Fitzgerald, "Hyperspectral imaging for early detection of oxygenation and perfusion changes in irradiated skin," J. Biomed. Opt. **17**(2), 026010 (2012).
15. L. C. L. Chin, E. K. Cook, D. Yohan, A. Kim, C. Niu, B. C. Wilson, and S. K. Liu, "Early biomarker for radiation-induced wounds: day one post-irradiation assessment using hemoglobin concentration measured from diffuse optical reflectance spectroscopy," Biomed. Opt. Express **8**(3), 1682–1688 (2017).
16. D. Yohan, A. Kim, E. Korpela, S. Liu, C. Niu, B. C. Wilson, and L. C. L. Chin, "Quantitative monitoring of radiation induced skin toxicities in nude mice using optical biomarkers measured from diffuse optical reflectance spectroscopy," Biomed. Opt. Express **5**(5), 1309–1320 (2014).
17. V. D. Thanik, C. C. Chang, R. A. Zoumalan, O. Z. Lerman, R. J. Allen, P. D. Nguyen, S. M. Warren, S. R. Coleman, and A. Hazen, "A Novel Mouse Model of Cutaneous Radiation Injury," Plast. Reconstr. Surg. **127**(2), 560–568 (2011).
18. U. Baran, W. J. Choi, and R. K. Wang, "Potential use of OCT-based microangiography in clinical dermatology," Skin. Res. Technol. **22**(2), 238–246 (2016).

19. W. J. Chen, Y. Y. Chang, S. C. Shen, Y. L. Tzeng, H. C. Lee, C. H. Yang, and M. T. Tsai, "In vivo detection of UV-induced acute skin effects using optical coherence tomography," Biomed. Opt. Express **9**(9), 4235–4245 (2018).

20. J. Qin, J. Y. Jiang, L. An, D. Gareau, and R. K. Wang, "In Vivo Volumetric Imaging of Microcirculation Within Human Skin Under Psoriatic Conditions Using Optical Microangiography," Lasers Surg. Med. **43**(2), 122–129 (2011).

21. A. J. Deegan, F. Talebi-Liasi, S. Z. Song, Y. D. Li, J. J. Xu, S. J. Men, M. M. Shinohara, M. E. Flowers, S. J. Lee, and R. K. K. Wang, "Optical coherence tomography angiography of normal skin and inflammatory dermatologic conditions," Lasers Surg. Med. **50**(3), 183–193 (2018).

22. P. Sharma, K. Sahu, P. K. Kushwaha, S. Kumar, M. K. Swami, J. Kumawat, H. S. Patel, S. Kher, P. K. Sahani, G. Haridas, and P. K. Gupta, "Noninvasive assessment of cutaneous alterations in mice exposed to whole body gamma irradiation using optical imaging techniques," Lasers Med. Sci. **32**(7), 1535–1544 (2017).

23. Y. Yoon, Q. Y. Li, V. H. Le, W. H. Jang, T. J. Wang, B. Kim, S. Son, W. K. Chung, C. Joo, and K. H. Kim, "Dark-field polarization-sensitive optical coherence tomography," Opt. Express **23**(10), 12874–12886 (2015).

24. A. S. Nam, I. Chico-Calero, and B. J. Vakoc, "Complex differential variance algorithm for optical coherence tomography angiography," Biomed. Opt. Express **5**(11), 3822–3832 (2014).

25. D. X. Hammer, A. Lozzi, E. Abliz, N. Greenbaum, A. Agrawal, V. Krauthamer, and C. G. Welle, "Longitudinal vascular dynamics following cranial window and electrode implantation measured with speckle variance optical coherence angiography," Biomed. Opt. Express **5**(8), 2823–2836 (2014).

26. W. J. Choi, K. L. Pepple, Z. W. Zhi, and R. K. Wang, "Optical coherence tomography based microangiography for quantitative monitoring of structural and vascular changes in a rat model of acute uveitis in vivo: a preliminary study," J. Biomed. Opt. **20**(1), 016015 (2015).

27. O. Goertz, C. Poettgen, A. Akbari, J. Kolbenschlag, S. Langer, M. Lehnhardt, M. Stuschke, and L. von der Lohe, "New model for long-term investigations of cutaneous microcirculatory and inflammatory changes following irradiation," J. Radiat. Res. **56**(3), 456–461 (2015).

28. T. A. Liu, J. Zhou, E. J. Yoshida, S. A. Woodhouse, P. B. Schiff, T. J. C. Wang, Z. F. Lu, E. Pile-Spellman, P. P. Zhang, and G. J. Kutcher, "Quantitative Ultrasonic Evaluation of Radiation-Induced Late Tissue Toxicity: Pilot Study of Breast Cancer Radiotherapy," Int. J. Radiat. Oncol., Biol., Phys. **78**(3), 811–820 (2010).

29. A. Warszawski, E. M. Rottinger, R. Vogel, and N. Warszawski, "20 MHz ultrasonic imaging for quantitative assessment and documentation of early and late postradiation skin reactions in breast cancer patients," Radiother. Oncol. **47**(3), 241–247 (1998).

30. H. P. Rodemann and M. A. Blaese, "Responses of normal cells to ionizing radiation," Semin. Radiat. Oncol. **17**(2), 81–88 (2007).

31. W. Wieser, B. R. Biedermann, T. Klein, C. M. Eigenwillig, and R. Huber, "Multi-Megahertz OCT: High quality 3D imaging at 20 million A-scans and 4.5 GVoxels per second," Opt. Express **18**(14), 14685–14704 (2010).

32. D. H. Choi, H. Hiro-Oka, K. Shimizu, and K. Ohbayashi, "Spectral domain optical coherence tomography of multi-MHz A-scan rates at 1310 nm range and real-time 4D-display up to 41 volumes/second," Biomed. Opt. Express **3**(12), 3067–3086 (2012).

33. G. L. Lu and B. W. Fei, "Medical hyperspectral imaging: a review," J. Biomed. Opt. **19**(1), 010901 (2014).

34. U. Morgner, W. Drexler, F. X. Kartner, X. D. Li, C. Pitris, E. P. Ippen, and J. G. Fujimoto, "Spectroscopic optical coherence tomography," Opt. Lett. **25**(2), 111–113 (2000).

35. S. P. Chong, C. W. Merkle, C. Leahy, H. Radhakrishnan, and V. J. Srinivasan, "Quantitative microvascular hemoglobin mapping using visible light spectroscopic Optical Coherence Tomography," Biomed. Opt. Express **6**(4), 1429–1450 (2015).

36. M. C. Skala, A. Fontanella, H. Hendargo, M. W. Dewhirst, and J. A. Izatt, "Combined hyperspectral and spectral domain optical coherence tomography microscope for noninvasive hemodynamic imaging," Opt. Lett. **34**(3), 289–291 (2009).

37. S. Dontu, S. Miclos, D. Savastru, and M. Tautan, "Combined spectral-domain optical coherence tomography and hyperspectral imaging applied for tissue analysis: Preliminary results," Appl. Surf. Sci. **417**, 119–123 (2017).